Exploring the role of electrode microstructure on the performance of non-aqueous redox flow batteries

Exploring the Role of Electrode Microstructure on the Performance of Non-Aqueous Redox Flow Batteries

Antoni Forner-Cuenca,[1,2,*] Emily E. Penn,[1,2] Alexandra M. Oliveira,[3] and Fikile R. Brushett[1,2,*,z]

[1] *Joint Center for Energy Storage Research, Massachusetts Institute of Technology, Cambridge, Massachusetts 02139, USA*
[2] *Department of Chemical Engineering, Massachusetts Institute of Technology, Cambridge, Massachusetts 02139, USA*
[3] *Department of Chemical & Biomolecular Engineering, University of Connecticut, Storrs, Connecticut 06269, USA*

Redox flow batteries are an emerging technology for long-duration grid energy storage, but further cost reductions are needed to accelerate adoption. Improving electrode performance within the electrochemical stack offers a pathway to reduced system cost through decreased resistance and increased power density. To date, most research efforts have focused on modifying the surface chemistry of carbon electrodes to enhance reaction kinetics, electrochemically active surface area, and wettability. Less attention has been given to electrode microstructure, which has a significant impact on reactant distribution and pressure drop within the flow cell. Here, drawing from commonly used carbon-based diffusion media (paper, felt, cloth), we systematically investigate the influence of electrode microstructure on electrochemical performance. We employ a range of techniques to characterize the microstructure, pressure drop, and electrochemically active surface area in combination with in-operando diagnostics performed in a single electrolyte flow cell using a kinetically facile redox couple dissolved in a non-aqueous electrolyte. Of the materials tested, the cloth electrode shows the best performance; the highest current density at a set overpotential accompanied by the lowest hydraulic resistance. We hypothesize that the bimodal pore size distribution and periodic, well-defined microstructure of the cloth are key to lowering mass transport resistance.

 [DOI: 10.1149/2.0611910jes]

Manuscript submitted March 1, 2019; revised manuscript received May 2, 2019. Published June 26, 2019. This was Paper 226 presented at the Seattle, Washington Meeting of the Society, May 13–17, 2018.

Electrochemical energy storage is anticipated to play a pivotal role in decarbonizing the electric sector by facilitating the reliable delivery of electricity generated from low-cost but intermittent renewable resources, enhancing the efficiency and flexibility of existing grid infrastructure, and bolstering system resilience to outages.[1] Redox flow batteries (RFBs) are a promising technology platform for low-cost, long-duration energy storage as, while more complex and less energy dense than enclosed batteries (e.g., Li-ion batteries), the system architecture enables improvements in scalability, service life, and safety.[2,3] While the all-vanadium RFB remains the current state-of-the-art system, the need for further cost reduction is driving research and development efforts into next-generation redox chemistries. This includes the exploration of non-aqueous electrolytes, which offer wider windows of electrochemical stability, as well as inexpensive redox couples based on organics and metal-centered coordination complexes with properties tailorable by molecular functionalization.[4–9] Although less well-represented in the literature, advances in reactor performance represent another pathway to cost reduction, as increased power density reduces the size of the electrochemical stack required to meet design specifications.[10]

Porous electrodes play an integral role in enabling RFB performance as they provide active surfaces for electrochemical reactions, distribute liquid electrolytes, cushion mechanical compression, and conduct electrons and heat.[11,12] As such, the electrodes contribute to charge transfer, ohmic, and mass transport overpotentials within the electrochemical cell.[13] Notably, most high-performance RFB reactors employ porous electrodes based on the fibrous carbon backing layers of polymer electrolyte fuel cell gas diffusion layers (GDLs).[13,14] While these materials are functional due to an overlap in desired property sets (e.g., permeability, electrical conductivity), they are not designed to meet all RFB requirements. In particular, flow battery electrodes must simultaneously enable facile redox reactions on the electrode surface area and facilitate liquid transport throughout the entirety of the architecture to ensure full utilization. The former is especially relevant with kinetically-limited systems (e.g., $k_0 < 10^{-5}$ cm s^{-1}) as most GDL backing layers have low surface areas (<10 m^2 g^{-1}) of ill-defined composition. As this is the case in all-vanadium RFBs,[15] considerable effort has been focused on modifying commercially available materials to increase active surface area, hydrophilicity, and/or catalytically-active surface functional groups. Indeed, a range of techniques including thermal activation,[16–20] acidic or basic treatment,[21–23] plasma activation,[24] and deposition of nanoparticles[25–27] have been successfully applied to carbon papers and felts, resulting in marked improvements in RFB performance due to reductions in charge transfer overpotential. While valid, these approaches are typically empirical, often relying on qualitative comparison of full cell polarization curves with pristine and modified materials, which belies the complex coupling of transport and reaction kinetics within the electrode that ultimately defines performance limits. Thus, in parallel, it is relevant to develop more generalized approaches to understanding the interplay between transport and reactions within porous electrodes using model redox couples with well-defined properties and electrochemical diagnostic platforms that enable disaggregation and quantification of the different overpotentials. Such approaches may enable the development of structure-function-performance relationships that inform the bottom-up design of advanced electrode microstructures directed to chemistries with particular property sets or to applications with particular performance needs.

The mass transport in RFBs is an area of growing interest and is increasingly recognized as a performance-limiting factor[28–31] for both aqueous[32] and non-aqueous systems.[29,33] Moreover, many emerging redox chemistries, particularly those based on organic couples,[34–36] have high kinetic rate constants ($k_0 > 10^{-3}$ cm s^{-1}), and thus reduced activation overpotentials which may obviate the need for modifications of the electrode surface, at least for the purpose of enhancing redox reaction rates. To date, most of the published literature on this topic has focused on understanding and optimizing flow field design,[28–30,37–39] though there have been some efforts to describe mass transport within given electrode materials[29,40] as well as to engineer electrode structure post-process. For example, Maryhuber et al. used a CO_2-laser to perforate SGL 10AA carbon papers and demonstrated improvements (up to 30%) in the power density of all-vanadium RFBs, which they ascribed to enhancements in electrolyte accessibility.[31,41] Using a similar approach, Dennison et al. evaluated the influence of electrode

*Electrochemical Society Member.
[z]E-mail: brushett@mit.edu

Table I. Electrodes used in this study and relevant physical properties.

ID Name	Commercial Name	Thickness* (mm)	$\varepsilon^{\#}$ (%)	ε_{MIP} (%)
SGL paper	Sigracet SGL 39AA	0.32 ± 0.01	91	88 ± 2
Toray paper	Toray TPG-H-120	0.35 ± 0.01	80	77 ± 2
Freudenberg paper	Freudenberg H23	0.21 ± 0.01	80	74 ± 1
Cloth	Nuvant ELAT Cloth	0.38 ± 0.01	82	78 ± 2
Felt	AvCarb Soft Graphite Felt	6.0 ± 0.1	95	91 ± 2

*Uncompressed electrode.
#Per vendor specification datasheet.

perforation in tandem with flow field design and found that, while pressure drop decreased, electrochemical performance was not improved when the perforated carbon paper was used in combination with an interdigitated flow field.[31] However, the flow in an interdigitated flow field (IDFF) is complicated, and the geometry must be carefully designed to ensure enhanced velocities and flow distribution in order to realize the full potential of this type of flow field.[42–44] Further, in the process of modifying the surface of different carbon papers and cloths via a KOH treatment, Zhou et al. observed differences in performance based on the electrode microstructure.[23,45,46] The authors attributed the improved performance in the woven electrodes to the broad pore size distribution, in particular the large, low tortuosity pores responsible for low pressure drop and high ionic conductivity. Building on these prior observations, we seek to evaluate the role of electrode microstructure on electrode performance in a RFB under well-controlled conditions that approximate practical operation.

Here, we systematically investigate the performance of select off-the-shelf carbon paper, felt, and cloth electrodes using complementary microscopic, analytical, and electrochemical techniques to correlate electrode microstructure and electrochemical performance. First, relevant physical properties of the electrode – microstructure and surface area – are determined using microscopy, mercury intrusion porosimetry, and double layer capacitance. Second, in-plane pressure drop is measured using a custom setup and bulk permeabilities are calculated from the resulting data. Third, to quantify resistive losses of each electrode, polarization and electrochemical impedance spectroscopy measurements are performed in a single electrolyte flow cell[42,47,48] containing a kinetically facile model organic redox couple, 2,2,6,6-tetramethylpiperidine-1-oxyl / 2,2,6,6-tetramethyl-1-oxo-piperidinium cation (TEMPO/TEMPO$^+$), dissolved in an acetonitrile-based electrolyte.[49] By coupling the electrochemical results with the pressure drop measurements, we observe different trends for the woven and non-woven materials. While this study focuses on non-aqueous electrolytes, the approach employed is broadly applicable to other RFB chemistries and may inform electrode development for other electrochemical technologies in which solution phase transport through porous media is relevant.

Experimental

Electrolyte preparation.—Solution preparation and electrochemical characterization were performed inside an argon filled glove box (MBraun, 4GB 2500, O_2 <5 ppm, H_2O <1 ppm). (2,2,6,6-Tetramethylpiperidin-1-yl)oxyl (TEMPO, 98+%, Alfa Aesar) was used as received. The oxidized form, 2,2,6,6-Tetramethyl-1-piperidinyloxy-oxo tetrafluoroborate (here, for simplicity, abbreviated as TEMPO$^+$), was prepared via a chemical oxidation[50] wherein 11 g of TEMPO were dissolved in acetonitrile (MeCN, 99.98%, BASF) followed by the slow addition of 1.1 molar equivalents of nitrosonium tetrafluoroborate ($NOBF_4$, 98%, Alfa Aesar) into the solution under a blanket of argon (Airgas, UHP, 99.999%). Afterwards, a rotary evaporator (Buchi R210) was used to remove the solvent and recover the synthesized solid. An oxidation conversion of 99.2% was obtained, as determined by microelectrode measurement (Figure S1). Tetraethylammonium tetrafluoroborate ($TEABF_4$, 99.99%, BASF) was used as received. For all electrochemical experiments, unless otherwise stated, the electrolyte solution consisted of 0.25 M TEMPO, 0.25 M TEMPO$^+$ (50% state of charge), and 1.0 M $TEABF_4$ all dissolved in MeCN.

Electrode materials.—Five different commercial electrodes were used: Sigracet SGL 39AA (Ion Power Inc.), Toray TPG-H-120 (Fuel Cell Earth), Freudenberg H23 (Fuel Cell Store), Nuvant ELAT Cloth (Fuel Cell Etc), and AvCarb Soft Graphite Felt (Fuel Cell Earth). Table I provides the uncompressed thicknesses and porosities for all the electrodes. Electrode thickness was determined with a digital caliper (Mitutoyo, Absolute AOS) and the measurement was repeated five times. Porosities were provided as part of the vendor specification sheet and also measured via mercury intrusion porosimetry (MIP). All the electrodes were used as received, without treatment.

Physical characterization.—The microstructure and morphology of the different electrodes were visualized by scanning electron microscopy (SEM). A Zeiss Merlin High-resolution SEM (Carl Zeiss AG, Germany) was used to capture images at various magnifications with an acceleration voltage of 5 keV, an aperture of 30 μm, and gun-to-sample distance of ca. 6.5 μm. MIP analyses were performed by the Micrometrics Instrument Center (Norcross, Georgia) using a AutoPore V 9600 employing ≥0.1 g electrode sample and a 5 cm^3 volume penetrometer. Pore diameters were calculated assuming a cylindrical shape and mercury-carbon contact angles of 130° (advancing and receding) to determine the pore size distribution (PSD). Bulk porosity was estimated by registering the mass of the material before and after full imbibition with mercury, assuming a complete pore filling. For these measurements, the uncertainty is based on error propagation of the volumetric (±0.05 cm^3) and pressure (±0.5 psi) sensors.

Flow cell experiments.—Electrochemical diagnostics were performed using a redox flow cell[48,51] operated in a single electrolyte configuration[47] as to enable comparative electrode analyses over a range of applied potentials and electrolyte flow rates but at steady state and with a fixed state of charge (SOC, 50%). The flow diffusers were machined from polypropylene (Adaptive Engineering Inc.) and the flow through flow fields (FTFF) were milled from 3.18 mm thick impregnated graphite (G347B graphite, MWI, Inc.). In a FTFF, forced convection of the liquid electrolyte leads to near unidirectional flow tangential to the flow field and the membrane. While, in practical embodiments, this can lead to undesirable pressure drops,[42] for fundamental studies, this configuration simplifies descriptions of transport within the electrode and allows for more accurate mapping of the permeability values obtained for pressure drop measurements to the electrochemical performance data. In all experiments, the same electrode type (Table I) was used in the anode and cathode compartments, one electrode per side, and all electrodes were compressed using Teflon gaskets (W. L. Gore & Associates, Inc. Newark, DE) to ensure leak-free operation across the range of electrolyte flowrates, reduce contact resistance between electrically-connected components, and define a cross-sectional area for fluid flow. As each electrode has a different thickness (Table I), exact matching of compression is difficult, which is the motivation for using ohmically-corrected data. Here, we compress the Freudenberg

paper with a single gasket; the SGL, and Toray papers as well as the cloth with two gaskets; and the felt with a 5 mm thick graphite spacer and two gaskets. The electrodes are compressed by 9 to 23% (Table S1). The geometric active area, 1.7 cm × 1.5 cm, is 2.55 cm^2. Celgard 2500 (25 μm thick, Fuel Cell Store) was used as a separator due to its low ohmic resistance and compatibility with MeCN-based electrolytes. During operation, the electrolyte solution is placed in a sealed perfluoroalkoxy alkane (PFA) jar (10 mL, Savillex) and delivered to the flow cell using a peristaltic pump (Masterflex L/S series) through PFA tubing (4 mm, Swagelok). All materials were selected due to their chemical compatibility with the electrolyte solution.

To account for differences in electrode thickness, performance was compared at the same superficial electrolyte velocity (v_e, m s^{-1}):[29,52]

$$v_e = \frac{Q}{t_e w_e} \quad [1]$$

Where Q is the volumetric flow rate (m^3 s^{-1}), t_e is the compressed electrode thickness (m), and w_e is the electrode width (m; here, 0.015 m). We note that some prior reports have chosen to describe electrolyte velocity as an average interstitial velocity by accounting for the electrode porosity in the equation above.[37,51] We elect not to do so here due to the uncertainty associated with porosity and its variation under compression for the different electrode materials.[53] Electrode performances are evaluated at four different electrolyte velocities, 0.5, 1.5, 5.0 and 20 cm s^{-1}, which correspond to a two order of magnitude range of volumetric flow rates, 0.87 mL min^{-1} to 75.60 mL min^{-1}. We were unable to study the felt electrode at 5.0 and 20 cm s^{-1} as the volumetric flow rate requirements (>250 mL min^{-1}) exceeded the capabilities of the experimental setup.

The polarization measurements were performed using an Arbin battery tester (FBTS-8) by potentiostatic holds of 30 s in 25 mV steps between 0 and 0.6 V, recording one data point per second. The average current and voltage were calculated for the final 50% of data points to approximate steady state conditions. Before data collection, all cells were conditioned by flowing electrolyte at 5 mL min^{-1} for 10 min to ensure component wetting and bubble removal, followed by a constant cell potential hold of 0.2 V for 20 min. Electrochemical impedance spectroscopy (EIS) was recorded using a Biologic VMP3 potentiostat at open circuit voltage (OCV), with an amplitude of 10 mV over a frequency range of 200 kHz to 10 mHz, averaging 6 points per decade.

Capacitance measurements.—To estimate electrochemically active surface area (ECSA) of the porous electrodes, the electrochemical double layer capacitance (EDLC) was experimentally measured,[54,55] in a similar single electrolyte redox flow cell setup as described in the previous section but with a blank electrolyte composed of 0.1 M $TEABF_4$ in MeCN and a Nafion 117 membrane (Fuel Cell Store, used as received). For all electrodes, a constant volumetric flow rate of 10 mL min^{-1} was used, as the measured capacitance was found to be independent of electrolyte velocity. Cyclic voltammetry (CV) was performed between −0.3 V and 0.3 V at 6 different scan rates (20, 50, 100, 200, 300, and 500 mV s^{-1}) and the current was recorded. As expected, a symmetric voltammogram exhibiting capacitive behavior (i.e., constant current independent of voltage) without faradaic events was observed under all conditions (Figure S2). The negative and positive non-Faradaic currents were extracted at 0 V and the average capacitive current (A), i_{EDLC}, was calculated as:[56]

$$i_{EDLC} = \frac{i_+ + |i_-|}{2} \quad [2]$$

The EDLC (F) was calculated using a linear fitting of i_{EDLC} vs. voltage scan rate according to:

$$i_{EDLC} = EDLC \frac{dV}{dt} \quad [3]$$

For each electrode set, we subtracted the *EDLC* measured with an empty cell, containing an open cavity between the membrane and flow field, defined by the gaskets, but without electrodes, to isolate the capacitance contributions of the porous electrodes. The ECSA (m^2 g^{-1}) was calculated as follows:

$$ECSA = \frac{EDLC}{C_{spec}\, m_e} \quad [4]$$

Where C_{spec} is the specific capacitance (F cm^{-2}) and m_e is the porous electrode mass (g). C_{spec} was obtained by performing CV measurements on a freshly polished glassy carbon electrode (3 mm, CH Instruments, Inc.) of known geometric surface area. The obtained C_{spec} ≈ 18.0 ± 0.3 μF cm^{-2} (Figure S3) was used to calculate an approximate *ECSA* of all electrodes studied. While differences in C_{spec} are expected between glassy carbon and various carbon fibers that make up the different electrodes, the relative values are representative of the ECSA and the obtained C_{spec} is in the range of previously reported values.[57,58]

Pressure drop measurements.—To measure pressure drop through different electrodes under relevant conditions (e.g., flow geometry, electrode compression), we developed a custom cell setup (Figure S4). The apparatus is similar to the flow cell configuration used for the electrochemical experiments except that the separator / membrane is replaced by a solid copper plate (3 mm thickness, McMaster) to prevent electrolyte leakage and to force the fluid to only travel through a half-cell (i.e., one side of the full cell) to ensure that a pressure drop through the electrode and independent of electrolyte crossover through the separator is measured. More specifically, each electrode is sandwiched between the FTFF and the solid plate using gaskets, identical to the electrochemical testing. To determine the pressure drop, pressure was measured at the inlet and outlet of the cell with digital pressure gauges (SSI Technologies 30 psi MG1-9V, ± 1%). To determine electrode-specific pressure drop, we subtracted the pressure drop of an empty cell, which accounted for <10% of the total measured pressure drop, to eliminate contributions from the housing and tubing. For simplicity, experiments were performed using MeCN solvent rather than the electrolyte solution as both fluids are Newtonian with similar surface tensions and thus have similar wetting properties. Pressure drop was measured over a volumetric flow rate range of 0−25 mL min^{-1}.

Results and Discussion

The majority of commercially available porous carbon electrodes consist of micrometric carbon fibers, typically synthesized by carbonization of polymer precursor (e.g., polyacrylonitrile), which are consolidated into a coherent structure. The methods used to assemble the fibers into electrodes give rise to the various materials classifications (paper, felt, cloth) each with different microstructure and, consequently, divergent physical properties (e.g., flexibility). We hypothesize that differences in electrode microstructure will impact reactant delivery to the fiber surfaces and that, by systematically characterizing a range of materials, performance-determining descriptors can be identified and subsequently leveraged to realize improved materials.

Electrode microstructures.—We first characterize the microstructure and morphology of the different electrodes using SEM (Figure 1) and MIP (Figure 2). Figure 1 shows micrographs of each electrode at various magnifications to highlight key features at different length scales. Despite similar bulk porosities (see Table I) and carbon fiber diameters (ca. 7–9 μm, Figures 1a1–1e3), there are noticeable differences in microstructure across the set of electrodes. The carbon papers are non-woven materials consisting of fibers held together by a binder (SGL, Toray) or other means (Freudenberg). The method of cohering the mass of fibers affects macroscopic properties as demonstrated by the differences in flexibility and compressibility of the papers. In all cases, the fibers have preferential in-plane orientation, due to the methods of assembly, but, within that plane, they appear randomly oriented. The SGL paper has the largest pores as well as a significant amount of rough graphitic binder, likely a residual product of the electrode carbonization process, which occupies a large fraction of the microscale pores and partially covers the carbon fibers. In comparison, the Toray paper has smaller pores and less binder that also appears smoother.

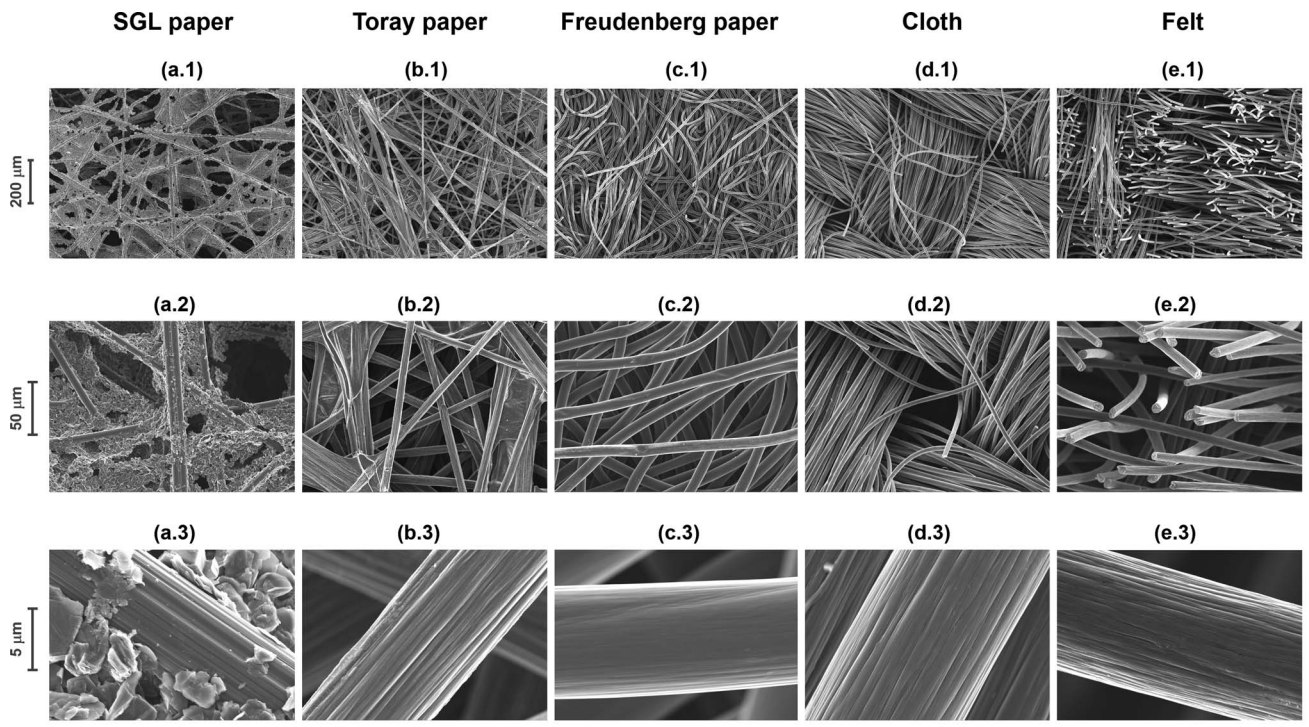

Figure 1. Scanning electron micrographs for the different electrodes used in this work: (a) SGL paper; (b) Toray paper; (c) Freudenberg paper; (d) Cloth; (e) Felt. Three different magnifications are shown.

The Freudenberg paper is assembled using a hydroentangling process driven by water jets that enables a binder-free mechanically-robust structure of randomly-organized curved fibers with small characteristic pores,[59] smaller than the other two papers. Higher magnification micrographs show striations on the surface of the carbon fibers of the SGL and Toray papers, whereas the carbon fibers of the Freudenberg paper appear smoother. We ascribe these differences to variations in processing conditions. Typically employed in earlier generation RFBs with flow-through flow fields, the felt electrode is an order of magnitude thicker than all other samples with relatively large pores. Similar to the Freudenberg paper, the felt electrode is binder-free, realizing structural integrity through fiber entanglement, which enables a flexible and compressible media. However, unlike the Freudenberg paper, the streaked carbon fibers which make up the felt are not randomly organized but rather appear to be loosely aligned in two preferential (and perpendicular) directions.

In contrast to the papers and felt, the carbon cloth derives its structural coherence from the systematic interworking of separate elements–each with their own structure make-up–in a particular weave pattern. In this context, an element is defined as a component part or unit of an interworked fabric (e.g., thread in sewing, yarn in knitting), which, here, we will refer to as a filament yarn. This approach is near ubiquitous in textile manufacturing as it enables the development of a broad array of materials, in terms of both form and function, with a diverse set of properties. The carbon cloth used in this study is a balanced plain weave, arguably the simplest of all interlacements, where the warp and weft filament yarns (ca. 100 carbon fibers) are aligned to form a criss-cross pattern. This structure leads to two distinct pore sets; namely, larger through-plane pores at the intersection between the yarns and smaller in-plane pores between the fibers within each element. Similar to the SGL and Toray papers, the carbon fibers of the cloth show striations.

To determine characteristic pore sizes for the different electrodes, MIP was used to obtain PSDs and assuming that mercury is a non-wetting fluid and that the pores are perfect cylinders of a given radius[60] (Figure 2). As qualitatively observed by SEM (see Figures 1a1), the SGL paper has a large average pore size, ca. 63 µm, with a smaller peak around 1–2 µm, which we tentatively attribute to the pores between graphite flakes in the binder and the carbon fibers. In comparison, the Toray and Freudenberg papers have smaller average pore sizes of 31 µm and 22 µm, respectively, with, in the case of the Toray paper, no clear contribution from the binder. The carbon felt electrode features a similar PSD as the SGL carbon paper with an average pore diameter around 60 µm. As mentioned before, the cloth has a bimodal PSD with large pores (ca. 85 µm diameter) and a notable fraction of smaller pores (ca. 10–15 µm diameter) which, respectively, correspond to the intersections between the woven elements and the void space between the fibers within each element. Note that MIP provides a semi-quantitative description of bulk PSD, which informs assessment of permeability and mass transport, but cannot resolve property variations within a sample. Previous studies have employed X-ray computed tomography (XTM) and shown directional dependence of GDL PSDs where pores are typically smaller in the in-plane direction, as compared to the through-plane direction, which, in turn, impacts directional permeabilities.[53,61–63] Such detailed characterization is beyond the scope of this work but will be contemplated in a future study.[64]

Electrode surface area.—To understand the impact of electrode microstructure on kinetic performance, we next evaluate the electrochemically active surface area of the different electrodes through analysis of the electrochemical double layer capacitance (EDLC). Electrode microstructure and morphology can impact accessible surface area which, in turn, can limit cell performance. While physical characterization methods such as MIP and nitrogen adsorption isotherms (e.g., Brunauer-Emmett-Teller (BET)) can also provide estimations of surface area, the operating principles of these analyses, the experimental conditions under which measurements are made, and the underlying assumptions made to extract the desired value are all substantially dissimilar to the intended electrochemical application.[65] As such, these methods may not provide as accurate a description of the electrochemically active surface area[57,65] In comparison, electrode

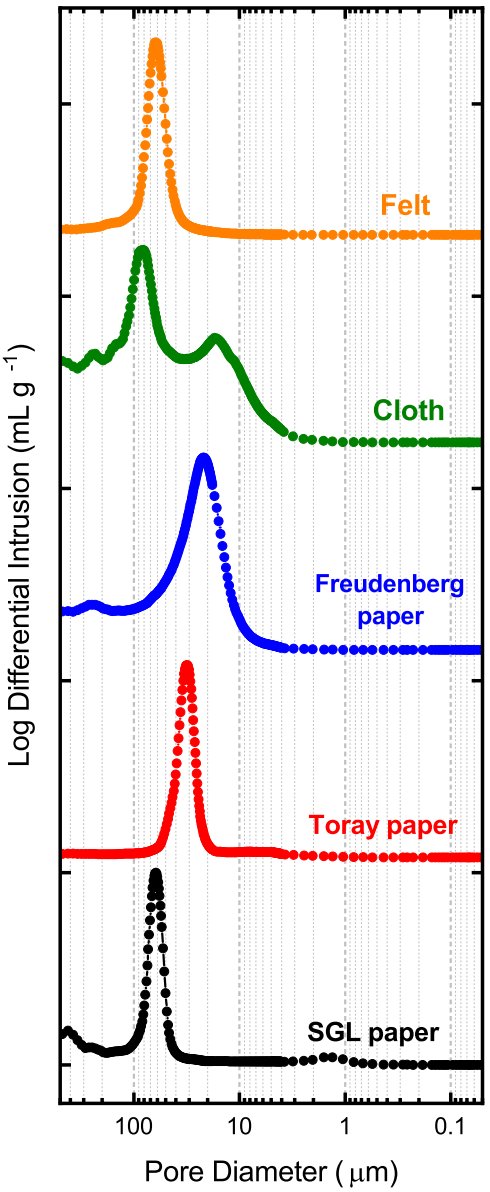

Figure 2. Pore size distribution curves of the different electrodes used in this study obtained with MIP.

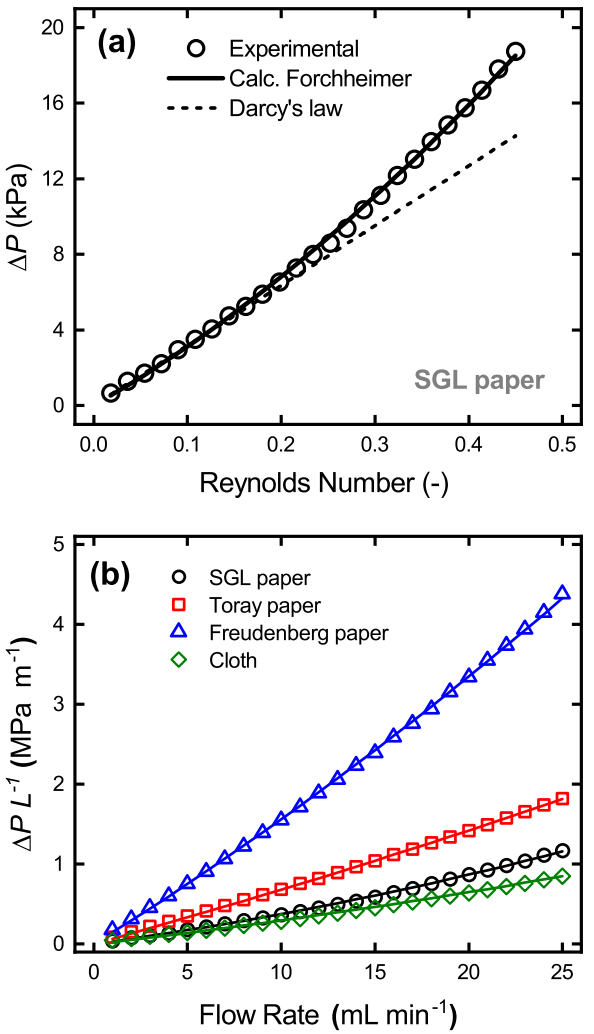

Figure 3. (a) Pressure drop vs. Reynolds number for SGL paper electrode showing the experimental data, the fitting using the Darcy-Forchheimer equation and the linear fitting using Darcy's law at low Re; (b) pressure drop per length vs. flow rate for the different electrodes showing experimental data and fitting using the Darcy-Forchheimer equation. Due to experimental limitations, the liquid pressure loss through the carbon felt electrode was measured employing water as a solvent and it is shown in Figure S5.

capacitance under flow provides a more relevant metric of available surface area as it is an electrochemical technique performed under conditions analogous to cell operation (Table II). The total capacitance is representative of the available wetted electrode surface area in a single electrolyte flow cell configuration; whereas, the specific surface area is normalize by the specific capacitance (assumed the same for all samples) and the respective electrode masses (different for all samples). Of the set, the Toray and Freudenberg papers and the carbon cloth have similarly lower capacitances, while the SGL carbon paper and carbon felt have relatively higher capacitances. Normalization reveals that the higher capacitance associated with the carbon felt is due to increased electrode mass (thicker sample), whereas the persistence of the high surface area for SGL reflects the contribution of the graphitic binder layer. Previous studies reported specific surface area values in the same order of magnitude for SGL materials.[16,65,66] For example, using a similar characterization method, Greco et al. estimated a specific surface area of 0.2 $m^2\ g^{-1}$ for pristine SGL 29AA in an aqueous acidic electrolyte.[16] We hypothesize that the slight variations in measured values are due to differences in electrolyte composition, which affect specific capacitance and electrode wetting, which impacts accessible area.

Related to the wetted surface area, the electrode utilization is impacted by the interaction between the electrolyte and the solid electrode and can be illustrated by the contact angle. Specifically, for a given electrolyte volume, an acute contact angle represents favorable interactions between the electrolyte and the electrode and thus maximal electrode utilization due to greater liquid spreading. In contrast, an obtuse contact angle indicates unfavorable interactions, thus poor wetting and reduced utilization absent of an additional energy

Table II. Measured capacitance and specific surface area of the electrodes used in this study.

ID Name	*EDLC* (μF)	*ECSA* ($m^2\ g^{-1}$)
SGL paper	1200 ± 100	0.50 ± 0.04
Toray paper	200 ± 20	0.029 ± 0.003
Freudenberg paper	620 ± 20	0.15 ± 0.01
Cloth	280 ± 20	0.050 ± 0.004
Felt	2800 ± 30	0.10 ± 0.01

input (e.g., greater pumping pressure). This is a known challenge for aqueous RFBs and there is an emerging body of work around improved wettability through modifications of carbon electrode surfaces.[66–70] However, better wettability is expected for organic solvents which have lower surface tensions than water (29.25 mN m^{-1} for MeCN/air[71] vs. 72.88 mN m^{-1} for water/air[72] at 293 K) and also lower contact angles when placed on a flat graphite surface (23 ± 3° for MeCN vs. 88 ± 5° for water, at room temperature and in air, Figure S4). Moreover, MeCN droplets applied externally were readily and rapidly imbibed into all the electrodes, that high electrode utilization is expected.[73] While a rigorous treatment is needed to quantitatively describe wetting of porous materials, based on this ex-situ evidence, it is reasonable to assume that MeCN fully wets the internal electrode surfaces. More generally, the improved wetting of organic solvents can be leveraged to enable better-performing non-aqueous electrochemical reactors that do not require extensive electrode pretreatments as well as to facilitate electrochemical diagnostics of porous electrodes where the non-aqueous electrolyte serves as a working fluid.

Pressure drop through electrodes .—We then quantify pressure drop through the different electrodes to compare hydraulic losses as a function of flow rate and to determine permeability, a materials-specific property. In prior fuel cell literature, electrode permeability is often estimated using the Carman-Kozeny equation, originally derived for flow through packed bed reactors[60] and modified to better capture the behavior in fiber beds.[74] However, the Carman-Kozeny equation is typically employed for fluid flows with higher Reynolds numbers (Re), as would be expected for gas flow in fuel cells but not for liquid flow in flow batteries. For low Re and unidirectional flow, the 1D Darcy's law can be used to described the relationship between pressure drop and fluid velocity:[75]

$$-\frac{dP}{dx} = \frac{\mu v}{k} \quad [5]$$

Where P is the pressure (Pa), x is the position coordinate (m), μ is the dynamic viscosity (Pa s), v is the superficial fluid velocity (m s^{-1}) and k is the material permeability (m^2). As shown in Figure 3a, Darcy's law aligns with experimental observations at low velocities where viscous forces dominate; however, deviations are observed at higher velocities as inertial forces begin to impact fluid behavior.[75,76] For the electrode materials considered here, the transition between Darcy and non-Darcy flow occurs at Re ≈ 0.05-0.20 in good agreement with previous studies of disordered fibrous media.[75–77] As such, we employ the 1D Darcy-Forchheimer equation[78] that includes an additional term to account for microscopic inertial effects:

$$-\frac{dP}{dx} = \frac{\mu v}{k} + \beta \rho v^2 \quad [6]$$

Where β is the non-Darcy or Forchheimer coefficient (m^{-1}), which accounts for inertial effects in the fluid flow, and ρ is the fluid density (kg m^{-3}). Defining an appropriate characteristic length scale within a fibrous electrode is challenging due to structural heterogeneity; thus, for convenience, fiber diameter or radius is typically selected.[79] Here, we employ a definition of Re, first proposed by Green and Duwez,[77] that incorporates material-specific microstructural information via the permeability and the non-Darcy coefficient:

$$Re = \frac{k\beta\rho v}{\mu} \quad [7]$$

Figure 3b shows the pressure drop per unit length as a function of electrolyte flow rate for four different electrodes, using MeCN as the working fluid. The observed pressure drops are inversely proportional to the PSD of the different electrodes (see Figure 2). Specifically, electrodes with the largest average pore diameters (SGL paper and cloth) experience the lowest pressure drops whereas the electrodes with the smallest average pore diameters (Freudenberg) experience the highest pressure drops. Notably, there is a more than five-fold difference between electrodes with the highest and lowest pressure drop, Freudenberg paper and cloth, respectively. Bulk permeabilities and non-Darcy coefficients are obtained by fitting the Darcy-Forchheimer model to experimental data and minimizing the square differences (Table III). As expected, the permeability values are directly proportional to the PSDs such that electrodes with larger pores have greater permeability and electrodes with smaller pores have lesser permeability. The range of permeability values measured is in general agreement with prior art[74,80–82] though, in many cases, quantitative comparisons are difficult due to application-specific material treatments, such as polytetrafluoroethylene (PTFE) coatings typical of PEFC GDLs, which may have a minor effect on permeability.[13,74] The Forchheimer coefficient indicates how the characteristic pressure drop deviates from the Darcy's law. As shown in Table III, this parameter is greater for SGL and Freudenberg papers than for Toray paper and cloth suggesting a slightly higher inertial contribution in the former two materials.

Table III. Calculated permeabilities and Forchheimer coefficient from experimental data fitting.

Electrode	$k \cdot 10^{11}$ (m^2)	$\beta \cdot 10^{-4}$ (m^{-1})
SGL paper	7.4 ± 1.4	3.2 ± 0.2
Toray paper	2.6 ± 0.1	2.0 ± 0.7
Freudenberg paper	2.0 ± 0.5	3.2 ± 1.0
Cloth	6.8 ± 0.4	2.1 ± 0.3
Felt*	2.7 ± 0.2	-

*Obtained using liquid water instead of MeCN and Equation 6 for fitting the data.

Note that as these measurements were performed in a flow cell setup with a FTFF, the permeability values are representative of in-plane transport. However, as evinced by the SEM images here and detailed in prior art,[40,61,63,74,81–83] these electrodes are anisotropic and substantial differences exist between in-plane and through-plane properties. Consequently, the flow field configuration is expected to impact the observed electrode permeability, particularly for interdigitated and serpentine flow fields with fluid velocity components in at least two directions.

Electrochemical performance.—Using a single electrolyte flow cell configuration,[29,47] we characterize the electrode performance and quantify resistive losses using a combination of cell polarization and electrochemical impedance spectroscopy (EIS) performed under steady-state conditions and at a constant 50% SOC (Figure 4). As illustrated in Figure 4a, during operation, electrolyte circulates through both electrodes with active species oxidizing on the anode and reducing on the cathode before returning to the reservoir. As this configuration uses a single redox couple, thus the same electrode reaction occurs in opposite directions on either side of the cell, the open circuit potential is zero and the cell potential measured upon the passage of current represents the summation of kinetic, ohmic, and transport resistances (Figure 4b). These individual resistances can be disaggregated using EIS and quantified through inspection or with a simple equivalent circuit model (Figure 4c). As we are interested in the role of transport phenomena in the performance of the different electrodes, we take steps to identify and minimize or eliminate kinetic and ohmic contributions, which convolute data analysis. Thus, we select a kinetically facile model redox couple, TEMPO/$TEMPO^+$, dissolved in a low viscosity organic solvent, MeCN, which also contains a moderate supporting salt concentration. Non-distributed area-specific ohmic resistance (R_Ω) is approximated from the high-frequency intercept from the Nyquist plot (Figure 4c) and this value is used to quantify and exclude ohmic contributions from polarization curve analysis (Figure 4b).[32] Across the electrode set, we measured R_Ω values of ca. 0.62 – 1.4 Ω cm^2, which is in general agreement with our prior work.[33] The range in these values is attributable to varying contact resistance contributions between the different electrodes and the graphite flow field, which may be due in part to the differences in the degree of mechanical compression (Table S1). For all experiments performed here, ohmic losses remain the largest contribution to total cell resistance as expected given the moderate

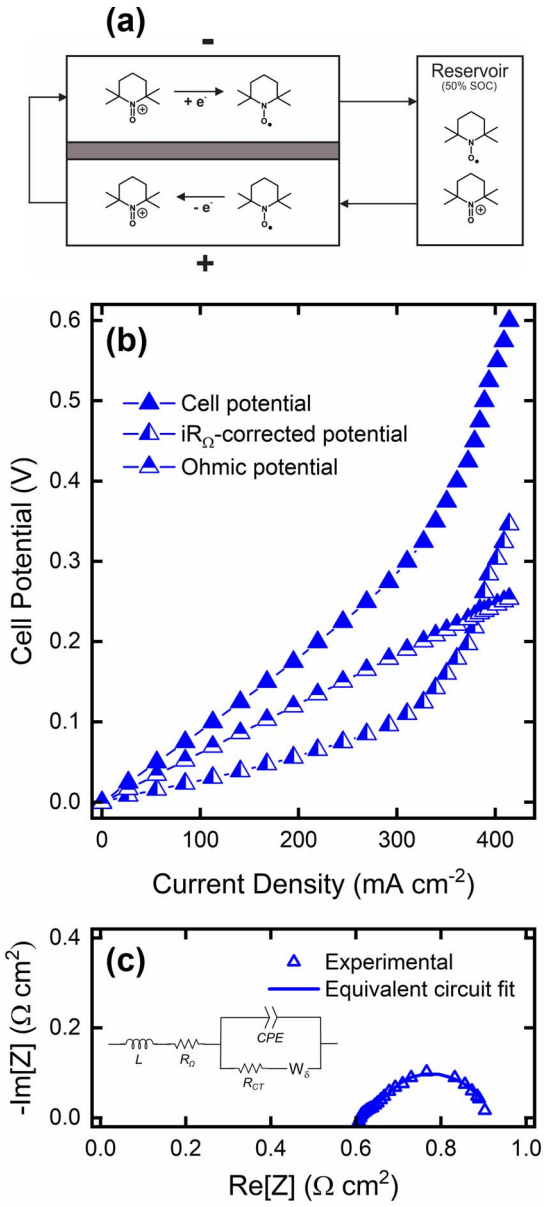

Figure 4. (a) Diagram of the single electrolyte flow cell configuration showing the redox active species, TEMPO and TEMPO$^+$. (b) Example cell polarization data using Freudenberg paper as the electrode material at a 2.62 mL min^{-1} flowrate ($v_e \approx 1.5$ cm s^{-1}). The ohmic contribution and the iR$_\Omega$-corrected cell voltage are also plotted. The state of charge was set to 50% (0.25 M TEMPO / 0.25 TEMPO$^+$). (c) Nyquist plots obtained using electrochemical impedance spectroscopy for different electrodes in a single electrolyte flow cell at open circuit potential under the same operating condition as in (b).

ionic conductivity of non-aqueous electrolytes.[5,33,84] We anticipate that kinetic contributions will be minor for all the electrodes tested as the TEMPO/TEMPO$^+$ redox couple has a high rate constant ($1.0 \times 10^{-1} > k_0 > 2.3 \times 10^{-2}$ cm s^{-1})[34,85] and is an outer sphere electron transfer reaction, therefore insensitive to electrode surface chemistry.[86] The magnitude of this contribution is difficult to estimate by inspection of the Nyquist plot in Figure 4c as the higher frequency kinetic and lower frequency mass transfer responses are convoluted. Thus, we employ a simple equivalent-circuit model consisting of an inductor (L), to account for the lead resistance, in series with an ohmic resistor (R$_\Omega$), as well as a constant-phase element (CPE), to account for the non-ideal capacitive effects of porous electrodes,[87,88] in parallel with a series charge transfer resistor (R_{CT}) and a bounded Warburg element (W_δ). The results of the fittings show that, as expected, the charge transfer resistance contributes < 5% of the total cell resistance and is significantly smaller than the mass transport resistance. A kinetic rate constant can be calculated from the estimated charge transfer resistance as follows:[89]

$$k_0 = \frac{i_0}{nFC_0} = \frac{RT}{(nF)^2 C_0 R_{CT}} \quad [8]$$

where i_0 is the exchange current density (A cm^{-2}), n is the number of electrons exchanged (here, n = 1), F is the Faraday constant (C mol^{-1}), and C_0 is the electrolyte bulk concentration (mol m^{-3}). The calculated values, which are tabulated in supporting information (Table S2), range from 2.5×10^{-3} to 4.1×10^{-2} cm s^{-1}, which are slightly lower than the previously reported values due to the relative coarseness of the estimation method.[34,85] Finally, we note that while EIS measurements at OCV serve as a useful point of comparison between different electrodes, quantitative descriptions of relative resistance contributions and their dependence on applied potentials are not captured.[90]

Electrode performance as a function of electrolyte velocity.— Increasing electrolyte flow rate to enhance mass transport is a common strategy used to improve electrochemical performance.[29,37,51,91,92] Here, we compare the different electrodes at common electrolyte velocities spanning two orders of magnitude via iR$_\Omega$-corrected polarization measurements (Figure 5) and electrochemical impedance spectroscopy (Figure 6). Due to pump limitations in our experimental setup, the thick felt electrode could only be evaluated at the lower two electrolyte velocities. At the lowest electrolyte velocity ($v_e \approx 0.5$ cm s^{-1}) limiting current densities were observed for all electrodes (Figure 5a), indicating reactant starvation. With increasing electrolyte velocity, advective transport is enhanced enabling faster active species replenishment and, as expected, significantly increases in limiting current density. Indeed, while a limiting current density is still observed for some of the electrodes at moderate electrolyte velocity ($v_e \approx$ 1.5 cm s^{-1}, Figure 5b), at the highest electrolyte velocities ($v_e \approx$ 5.0 cm s^{-1}, Figure 5c and $v_e \approx 20$ cm s^{-1}, Figure 5d), the polarization curves are linear over the range of current densities measured. While the degree of electrochemical performance improvement varies between electrodes, in all cases, there are diminishing returns for increasing electrolyte velocity. We hypothesize that, as the flow rate increases, the cells approach the limit of infinitely fast mass transfer and charge transfer losses dominate the resistive characteristics of the iR$_\Omega$-corrected polarization curve.

To quantify the resistive contributions to cell polarization as a function of electrolyte velocity, we evaluate flow rate-dependent impedance responses to a cell containing cloth electrodes as an exemplar (Figure 6a). As expected, increasing electrolyte velocities leads to a reduction in mass transfer resistance as evinced by the decreasing magnitude of the Nyquist plots. This in turn lowers cell resistance and thus decreases iR$_\Omega$-corrected cell polarization enabling access to higher current densities (Figure 5).[29] More specifically, for the cloth, mass transport overpotential accounts for ca. 35% of the total ASR ($R_{MT} \approx 0.51$ Ω cm^2) at low velocities and decreases to < 2% of the total ASR ($R_{MT} \approx 14$ mΩ cm^2) at the highest velocity which is on the same order as the charge-transfer resistance ($R_{CT} \approx 13$ mΩ cm^2). Qualitatively similar trends are observed for the other electrodes in the set and this data can be found in the supporting information (Figure S6 and Table S2). In all cases, R_Ω is independent of velocity, as expected. However, R_{CT} does vary with velocity, which is because the average concentration of reactant varies with the flow rate (i.e., stoichiometry).

As anticipated, for all electrodes, increasing electrolyte flow rate improves overall cell performance, higher current densities are achieved at a fixed cell potential, but the relative magnitudes of cell resistance as well as the extent and rate of resistance reduction with increasing electrolyte flowrate vary between the different electrodes. With an exception of the lowest electrolyte velocity, SGL and Toray carbon papers are the worst performing electrode materials. Of particular note is the inferior performance of the SGL carbon paper, which has both the highest ECSA due to the presence of graphite binder (Table II), as well as the highest bulk permeability, based on the largest characteristic pore size (Table III and Figure 2). This result suggests

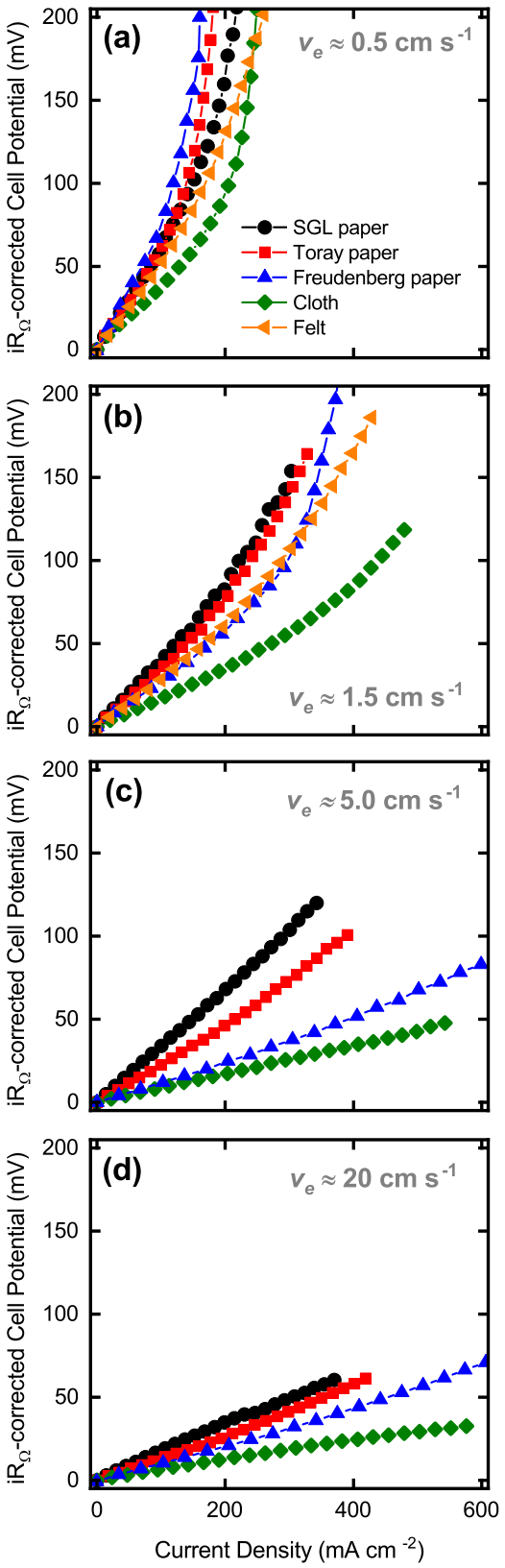

Figure 5. iR$_\Omega$-corrected cell potential versus current densities at 4 electrolyte velocities: (a) 0.5 cm s^{-1}, (b) 1.5 cm s^{-1}, (c) 5.0 cm s^{-1}, and (d) 20 cm s^{-1} for all five different electrodes at the lower velocities and four different electrodes at the higher velocities. For the felt electrode, the volume flowrates required to achieve the higher velocities exceeded the capabilities of the experimental apparatus. The state of charge was set to 50% (0.25 M TEMPO / 0.25 M TEMPO$^+$).

that high surface area is not beneficial to performance under these conditions and appears to indirectly support our earlier assertion that charge transfer losses are a minor contributor to cell resistance due to the electrolyte composition selected. For the carbon papers, electrode performance is inversely correlated to pore size as the Freudenberg paper outperforms both the SGL and Toray papers and shows greater sensitivity to electrolyte flow rate. Electrodes with smaller pores enable higher local electrolyte velocities, though similar superficial velocities, and shorter diffusion lengths to the electrode surface which, in turn, enhance electrochemical performance. In contrast, in electrodes with larger pores, greater volumes of electrolyte solution can pass through the porous material without contacting the electrode surface. Interestingly, while only lower flow rates can be explored due its thickness, the felt slightly outperforms the best papers at 0.5 cm s^{-1} and 1.5 cm s^{-1} despite having a relatively large characteristic pore size (Figure 2) suggesting that this parameter alone is not sufficient to describe performance sensitivity. Indeed, in addition to having similar pore sizes than the other papers, Freudenberg paper also has a distinct microstructure (Figure 1), more similar to that of the felt, in which entangled carbon fibers enable coherence without the need for binders. The cloth, which outperforms all other materials across the range of electrolyte velocities tested, also achieves structural integrity through the interworking of fibers that leads to bimodal PSDs, with large pores similar to the SGL paper and smaller pores similar to the Freudenberg paper, as well as alignment on the fiber and yarn length scales. Thus, the combination of the hierarchical organization and characteristic pore sizes appears to lead to the best electrochemical performance.

To quantify the resistive contributions to cell polarization for different electrodes, we compare impedance responses for cells containing the different electrode materials at a representative electrolyte velocity ($v_e \approx 1.5$ cm s^{-1}, Figure 6b). Similar data sets at different electrolyte velocities can be found in the supporting information (Figures S6 and Tables S2). The Nyquist plots show reduced resistance for cells containing the cloth, felt, and Freudenberg papers as compared to the SGL and Toray carbon papers, in general agreement with the polarization data (Figure 5). While the variations in cell resistance can be directly correlated to changes in mass transport resistance between the different electrodes, the SGL paper exhibits a higher-than-expected charge transfer resistance, especially considering its high ECSA. We hypothesize that this may be due to limited accessibility of electrode area (e.g., dead-end pores, channeling within the electrode) during cell operation which is supported by qualitative in situ imaging by Wong et al.[93] However, further work is needed to obtain a detailed understanding of intra-electrode transport and kinetics.

Balancing electrochemical performance with pressure drop.— For efficient system operation, the flow battery must balance the competing effects of power performance, enabled by increasing electrolyte flowrate through the porous electrodes, and pumping losses, associated with hydraulic resistance of the electrode (Figure 7). We anticipate that different electrode microstructures will lead to different optima, but the common overarching goal is to maximize power output without incurring offsetting pumping losses. Figure 7a illustrates this trade-off for woven (cloth) and non-woven (paper and felt) electrodes where pressure drop per unit length is plotted against the current density for a fixed iR-corrected overpotential of 50 mV, which aligns with expected overpotentials allowable for energy-efficient charge/discharge cycling.[3,94] On this graph, each data point represents a different electrolyte velocity (0.5, 1.5, 5, and 20 cm s^{-1}). The cloth provides the best balance of pressure drop and achievable current density; for example, ~570 mA cm^{-2} are obtained with a 0.50 MPa m^{-1} pressure loss. Of the papers, the Freudenberg paper demonstrates the second highest achieved current density (465 mA cm^{-2}); however, at a substantially greater pressure drop (9.8 MPa m^{-1}) suggesting that while increased electrochemical performance may be possible as compared to the cloth, the concomitant pumping requirements may preclude use of the Freudenberg paper under these conditions. Interestingly, for the carbon papers, there are diminishing returns with high flow rates (Figure 5). Though only two points are recorded due

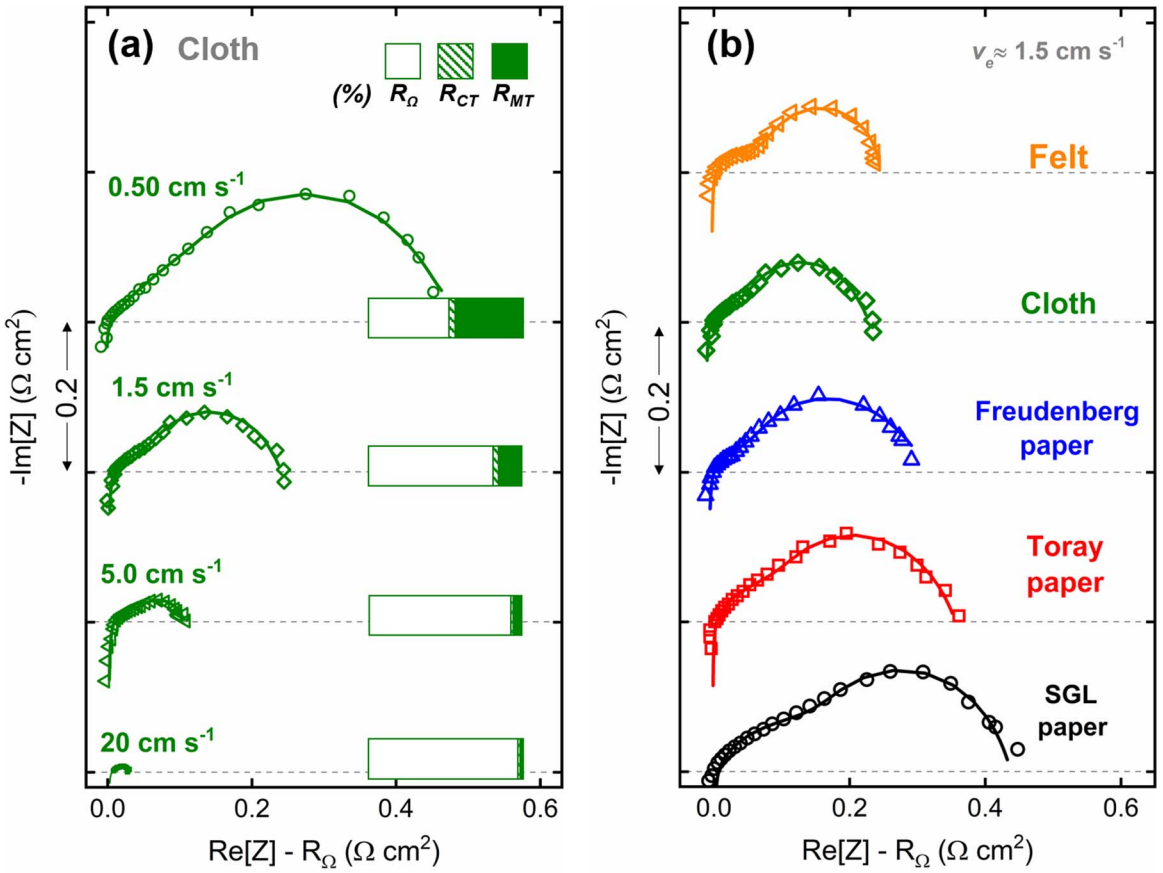

Figure 6. Nyquist plots obtained using electrochemical impedance spectroscopy for different electrodes in a single electrolyte flow cell at open circuit potential: (a) Carbon cloth electrode at four different electrolyte velocities (0.5, 1.5, 5.0, and 20 cm s^{-1}) and (b) five different electrodes at a given representative electrolyte velocity (1.5 cm s^{-1}).

to pumping limitations, the felt shows a similar trajectory to the cloth albeit at lower current densities. Figure 7b provides a different representation of this trade-off by comparing pumping power, determined for the electrode length in the experiments and calculated by multiplying the electrode-specific volumetric flow rate and pressure drop, and mass-transport-associated electric power, calculated by multiplying the fixed iR_Ω-corrected cell potential (50 mV) with the various current densities. The electric power represents an incremental power boost associated with mass transport whose relative magnitude is meaningful when comparing the different electrodes but the absolute magnitude does not as the voltage used is not characteristic of a practical RFB cell voltage. A parity line is used to indicate the limits of increasing electrolyte velocity for the different electrodes. Not only does the cloth electrode show the best balance of electrochemical performance and pressure drop across all electrolyte velocities tested but, the trade-off between mass-transport-related power and pumping power never exceeds unity suggesting that further increases in electrolyte flowrates may still yield improved performance. In contrast, the papers all show an unfavorable trade-off at the highest flow rates indicating an upper limit of electrolyte velocity, which is inversely dependent on characteristic pore size but significantly lower than that of the cloth. Although only two data points at low electrolyte velocities could be gathered due to volumetric flow rate limitations, the felt appears to be following an unfavorable trajectory as its increased thickness as compared to the other materials necessitates higher volumetric flow rates to achieve similar electrolyte velocities, directly contributing to pumping power requirements.

While others have postulated the advantage of bimodal PSDs,[23,41] to the best of our knowledge, this study is the first to systematically investigate the impact of electrode microstructure on mass transfer. We hypothesize that the hierarchical microstructure of the cloth electrode facilitates mass transport due to a combination of bimodal PSD, weave pattern, and fiber alignment. Specifically, the reduced mass transport resistance is facilitated by the presence of large pores with low tortuosity that enable high permeability and thus provide fast electrolyte replenishment, along with the small, aligned pores between the fibers within the filament yarns that enable high diffusive fluxes to the fiber surfaces. In addition, the narrow PSDs for each pore population and the periodic microstructure (Figure 2) may enable more uniform velocity distribution throughout the electrode while minimizing stagnation zones. Establishing quantitative design criteria for future electrodes based on the results described above requires a comprehensive treatment of the coupled reaction and transport processes within the specific three-dimensional electrode structures,[53,95–99] which is beyond the scope of this initial work.

Conclusions

Improving electrode performance within the electrochemical stack of an RFB offers a means of reducing system costs through decreased resistance and increased power density. While most prior work has focused on tuning surface chemistry to enhance redox reaction rates, comparatively few efforts have explored the role of electrode microstructure and its impact on mass transport and hydraulic resistance within the flow cell. To this end, we evaluated a series of electrodes (papers, felts, cloth), all based on micrometric carbon fibers of similar diameters but assembled into coherent structures via different methods, using a suite of microscopic, analytical, and electrochemical methods to develop structure-performance relationships. To minimize complications of carbon surface chemistry, electrode wetting, and variable contact resistance, ohmically-corrected polarization and electrochemical impedance spectroscopy measurements were performed in a single electrolyte flow cell configuration with a MeCN-based electrolyte

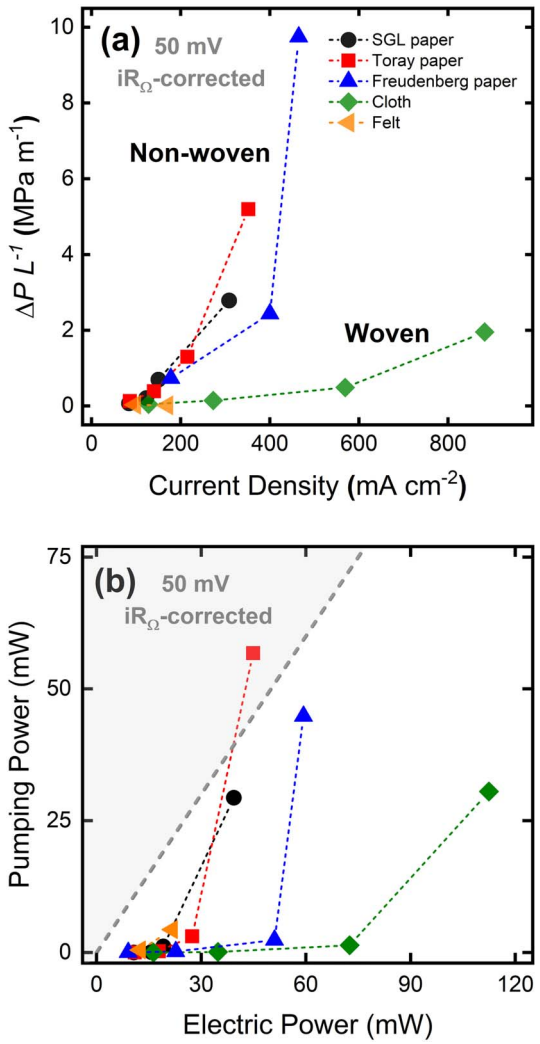

Figure 7. (a) Normalized pressure drop versus current density and (b) required pumping power versus electrical power at 50 mV iR$_\Omega$-correct overpotential for the five different electrodes. A demarcation of unity is indicated by the dashed line and the shaded region above this line.

containing a TEMPO/TEMPO$^+$ redox couple. In general, for the carbon papers, we found an inverse relationship between pore size distribution or permeability and electrochemical performance, where Freudenberg paper outperformed both Toray and SGL papers, and that the gains in mass transport offset the increases in hydraulic resistance. The felt electrode showed promising performance at low electrolyte velocities, but, as it is an order of magnitude thicker than the other electrodes, the volumetric flow rate requirements challenged our experimental apparatus and led to greater pumping losses. In contrast to the papers and felt, the hierarchical and periodic structure of the cloth electrode results in two distinct pore sets; specifically, larger through-plane pores at the perpendicular intersection of filament yarns and smaller in-plane pores between the fibers which make up each yarn. This bimodal distribution enables both high permeability, thus low hydraulic resistance, and low mass transfer resistance, thus high electrochemical performance, breaking the inverse relationship observed in electrodes with monomodal pore size distribution. This outcome is durable and applicable to different soluble redox chemistries though the relative impact of improved mass transfer on overall cell resistance will depend on the performance-limiting factors of the particular device.

Looking forward, the myriad of weave patterns associated with textile manufacturing provides nearly unlimited design opportunities for cloth electrodes. However, to efficiently progress through this materials space will require a more detailed understanding of local transport phenomena with the complex electrode geometry. Thus, future work will focus on combining electrochemical experiments with high-resolution imaging (e.g., X-ray tomographic microscopy) and computational fluid dynamic modeling, which can offer insights into electrolyte velocity and concentration distribution within different electrodes. In addition, though not the primary focus of this study, the reductions in mass transfer resistance as a function of electrode choice and electrolyte velocity enabled total cell resistances below 1 Ω cm^2 marking another important incremental step towards high power non-aqueous RFBs as current densities in excess of 400 mA cm^{-2} are achieved with 0.3 V of overpotential. However, continued efforts to develop redox chemistries with high cell voltage (≈3 V) and conductive yet sufficiently selective separators are necessary to ultimately realize a full high power system. While the focus of this study is non-aqueous electrolytes for use in RFBs, the outcomes should be generalizable to electrochemical technologies that leverage convective liquid-phase transport through reactive porous media.

Acknowledgments

We gratefully acknowledge the financial support of the Swiss National Science Foundation (P2EZP2_172183) and the Joint Center for Energy Storage Research (JCESR), an Energy Innovation Hub funded by the United States Department of Energy. The authors appreciate the valuable support from the members of the Brushett Lab at the Massachusetts Institute of Technology, particularly Jeffrey Kowalski for assistance in compound synthesis, and Katharine Greco, Charles Tai-Chieh Wan, Kevin Tenny, and McLain Leonard for manuscript preparation.

List of Symbols

Symbol	Description	Units
C_0	Bulk concentration	mol m^{-3}
C_{spec}	Specific capacitance	F cm^{-2}
E_{cell}	Cell voltage	V
ECSA	Electrochemically active surface area	m g^{-1}
EDLC	Electrochemical double-layer capacitance	F
F	Faraday constant	C mol^{-1}
i	Current density	mA cm^{-2}
i_0	Exchange current density	mA cm^{-2}
i_{EDLC}	Average capacitive current	mA
k	Permeability	m^2
k_0	Kinetic rate constant	cm s^{-1}
L	Inductance	H
m_e	Electrode mass	g
n	Number of electrons exchanged	-
P	Pressure	Pa
Q	Volumetric flow rate	m^3 s^{-1}
R_{CT}	Charge transfer area-specific resistance	Ω cm^2
Re	Reynolds number	-
R_{MT}	Mass transport area-specific resistance	Ω cm^2
R_P	Pore radius	m
R_Ω	Ohmic area-specific resistance	Ω cm^2
t	time	s
t_e	Electrode thickness	m
V	Voltage	V
v	Superficial fluid velocity	m s^{-1}
v_e	Electrolyte velocity	m s^{-1}
w_e	Electrode width	m
x	Position coordinate	m
	Greek	
β	Forchheimer coefficient	m^{-1}
ε	Porosity	-
η	Overpotential	V
η_{CT}	Charge transfer overpotential	V
η_{MT}	Mass transport overpotential	V
η_Ω	Ohmic overpotential	V
μ	Dynamic viscosity	Pa s
ρ	Fluid density	kg m^{-3}

ORCID

Antoni Forner-Cuenca https://orcid.org/0000-0002-7681-0435
Fikile R. Brushett https://orcid.org/0000-0002-7361-6637

References

1. S. Chu and A. Majumdar, Opportunities and challenges for a sustainable energy future. *Nature*, **488**, 294 (2012).
2. M. Skyllas-Kazacos, M. H. Chakrabarti, S. a. Hajimolana, F. S. Mjalli, and M. Saleem, Progress in Flow Battery Research and Development. *J. Electrochem. Soc.*, **158**, R55 (2011).
3. A. Z. Weber et al. Redox flow batteries: A review. *J. Appl. Electrochem.*, **41**, 1137 (2011).
4. R. M. Darling, K. G. Gallagher, J. A. Kowalski, S. Ha, and F. R Brushett, Pathways to low-cost electrochemical energy storage: a comparison of aqueous and nonaqueous flow batteries. *Energy Environ. Sci.*, **7**, 3459 (2014).
5. R. Dmello, J. D. Milshtein, F. R. Brushett, and K. C. Smith, Cost-driven materials selection criteria for redox flow battery electrolytes. *J. Power Sources*, **330**, 261 (2016).
6. J. D. Milshtein, R. M. Darling, J. Drake, M. L. Perry, and F. R. Brushett, The Critical Role of Supporting Electrolyte Selection on Flow Battery Cost. *J. Electrochem. Soc.*, **164**, A3883 (2017).
7. C. Minke, U. Kunz, and T. Turek, Techno-economic assessment of novel vanadium redox flow batteries with large-area cells. *J. Power Sources*, **361**, 105 (2017).
8. B. M. L. Perry, Expanding the chemical space for redox flow batteries. *Science (80-.).*, **503**, 3459 (2015).
9. J. A. Kowalski, L. Su, J. D. Milshtein, and F. R. Brushett, Recent advanced in molecular engineering of redox active organic molecules for nonaqueous flow batteries. *Curr. Opin. Chem. Eng.*, **13**, 45 (2016).
10. M. L. Perry, R. M. Darling, and R. Zaffou, High Power Density Redox Flow Battery Cells, *ECS Trans*. **53**, 7 (2013).
11. D. Aaron, Z. Tang, A. B. Papandrew, and T. A. Zawodzinski, Polarization curve analysis of all-vanadium redox flow batteries. *J. Appl. Electrochem.*, **41**, 1175 (2011).
12. W. Wang et al. Recent progress in redox flow battery research and development. *Adv. Funct. Mater.*, **23**, 970 (2013).
13. M. F. Mathias, J. Roth, J. Fleming, and W Lehnert, Diffusion media materials and characterisation. *Handb. Fuel Cells*, **3**, 517 (2010).
14. M. H. Chakrabarti et al. Application of carbon materials in redox flow batteries. *J. Power Sources*, **253**, 150 (2014).
15. K. J. Kim et al. A technology review of electrodes and reaction mechanisms in vanadium redox flow batteries. *J. Mater. Chem. A*, **3**, 16913 (2015).
16. K. V Greco, A. Forner-Cuenca, A. Mularczyk, J. J. Eller, and F. R. Brushett, Elucidating the Nuanced Effects of Thermal Pretreatment on Carbon Paper Electrodes for Vanadium Redox Flow Batteries. *ACS Appl. Mater. Interfaces*, **10**, 44430 (2018).
17. N. Pour et al. Influence of Edge- and Basal-Plane Sites on the Vanadium Redox Kinetics for Flow Batteries. *J. Phys. Chem. C*, **119**, 5311 (2015).
18. A. M. Pezeshki, J. T. Clement, G. M. Veith, T. A. Zawodzinski, and M. M. Mench, High performance electrodes in vanadium redox flow batteries through oxygen-enriched thermal activation. *J. Power Sources*, **294**, 333 (2015).
19. S. M. Taylor et al. Vanadium (V) reduction reaction on modified glassy carbon electrodes - Role of oxygen functionalities and microstructure. *Carbon N. Y.* **109**, 472 (2016).
20. Y. Shao et al. Nitrogen-doped mesoporous carbon for energy storage in vanadium redox flow batteries. *J. Power Sources*, **195**, 4375 (2010).
21. Y. Kim, S. Cho, S.-K. Park, J.-D. Jeon, and Y.-S. Lee, Electrochemical properties of carbon felt electrode for vanadium redox flow batteries by liquid ammonia treatment. *Appl. Chem. Eng.*, **25**, 292 (2014).
22. T. Wu et al. Hydrothermal ammoniated treatment of PAN-graphite felt for vanadium redox flow battery. *J. Solid State Electrochem.*, **16**, 579 (2012).
23. X. L. Zhou, T. S. Zhao, Y. K. Zeng, L. An, and L. Wei, A highly permeable and enhanced surface area carbon-cloth electrode for vanadium redox flow batteries. *J. Power Sources*, **329**, 247 (2016).
24. K. J. Kim, Y. J. Kim, J. H. Kim, and M. S. Park, The effects of surface modification on carbon felt electrodes for use in vanadium redox flow batteries. *Mater. Chem. Phys.*, **131**, 547 (2011).
25. L. Wei, T. S. Zhao, G. Zhao, L. An, and L. Zeng, A high-performance carbon nanoparticle-decorated graphite felt electrode for vanadium redox flow batteries. *Appl. Energy*, **176**, 74 (2016).
26. L. Wei, T. S. Zhao, L. Zeng, X. L. Zhou, and Y. K. Zeng, Copper nanoparticle-deposited graphite felt electrodes for all vanadium redox flow batteries. *Appl. Energy*, **180**, 386 (2016).
27. B. Li et al. Bismuth nanoparticle decorating graphite felt as a high-performance electrode for an all-vanadium redox flow battery. *Nano Lett.* **13**, 1330 (2013).
28. K. M. Lisboa et al. Mass transport enhancement in redox flow batteries with corrugated fluidic networks. *J. Power Sources*,**359**, accepted (2017).
29. J. D. Milshtein et al. Quantifying Mass Transfer Rates in Redox Flow Batteries. *J. Electrochem. Soc.*, **164**, E3265 (2017).
30. J. Houser, A. Pezeshki, J. T. Clement, D. Aaron, and M. M. Mench, Architecture for improved mass transport and system performance in redox flow batteries. *J. Power Sources*, **351**, 96 (2017).
31. C. R. Dennison, E. Agar, B. Akuzum, and E. C. Kumbur, Enhancing Mass Transport in Redox Flow Batteries by Tailoring Flow Field and Electrode Design. *J. Electrochem. Soc.*, **163**, A5163 (2015).
32. A. M. Pezeshki, R. L. Sacci, F. M. Delnick, D. S. Aaron, and M. M. Mench, Elucidating effects of cell architecture, electrode material, and solution composition on overpotentials in redox flow batteries. *Electrochim. Acta*, **229**, 261 (2017).
33. J. D. Milshtein et al. Towards Low Resistance Nonaqueous Redox Flow Batteries. *J. Electrochem. Soc.*, **164**, A2487 (2017).
34. Y. Yonekuta, K. Oyaizu, and H. Nishide, Structural Implication of Oxoammonium Cations for Reversible Organic One-electron Redox Reaction to Nitroxide Radicals. *Chem. Lett.*, **36**, 866 (2007).
35. X. Wei et al. Towards high-performance nonaqueous redox flow electrolyte via ionic modification of active species. *Adv. Energy Mater.*, (2015).
36. C. Buhrmester, L. Moshurchak, R. L. Wang, and J. R. Dahn, Phenothiazine Molecules: Possible Redox Shuttle Additives for Chemical Overcharge and Overdischarge Protection for Lithium-Ion Batteries. *J. Electrochem. Soc.*, **153**, A288 (2006).
37. X. You, Q. Ye, and P. Cheng, The Dependence of Mass Transfer Coefficient on the Electrolyte Velocity in Carbon Felt Electrodes: Determination and Validation. *J. Electrochem. Soc.*, **164**, E3386 (2017).
38. A. Bhattarai et al. Advanced porous electrodes with flow channels for vanadium redox flow battery. *J. Power Sources*, **341**, 83 (2017).
39. A. Tang, J. Bao, and M. Skyllas-Kazacos, Studies on pressure losses and flow rate optimization in vanadium redox flow battery. *J. Power Sources*, **248**, 154 (2014).
40. Q. Xu and T. S. Zhao, Determination of the mass-transport properties of vanadium ions through the porous electrodes of vanadium redox flow batteries. *Phys. Chem. Chem. Phys.*, **15**, 10841 (2013).
41. I. Mayrhuber, C. R. Dennison, V. Kalra, and E. C. Kumbur, Laser-perforated carbon paper electrodes for high-power vanadium redox flow batteries (Abstract). *225th ECS Meet*. **260**, 251 (2014).
42. R. M. Darling and M. L. Perry, The Influence of electrode and channel configurations on flow battery performance. *J. Electrochem. Soc.*, **161**, A1381 (2014).
43. M. MacDonald and R. M. Darling, Modeling flow distribution and pressure drop in redox flow batteries. *AIChE J.* **64**, 3746 (2018).
44. M. Macdonald and R. M. Darling, Comparing velocities and pressures in redox flow batteries with interdigitated and serpentine channels. *AIChE J.* **65**, e16553 (2019).
45. X. L. Zhou, Y. K. Zeng, X. B. Zhu, L. Wei, and T. S. Zhao, A high-performance dual-scale porous electrode for vanadium redox flow batteries. *J. Power Sources*, **325**, 329 (2016).
46. X. L. Zhou, T. S. Zhao, L. An, Y. K. Zeng, and L. Wei, Critical transport issues for improving the performance of aqueous redox flow batteries. *J. Power Sources*, **339**, 1 (2017).
47. R. M. Darling and M. L. Perry, *Pseudo-Steady-State Flow Battery Experiments.*, in *ECS Transactions Abstract #480* (2013).
48. J. D. Milshtein, J. L. Barton, R. M. Darling, and Brushett, F. R. 4-Acetamido-2,2,6,6-Tetramethylpiperidine-1-Oxyl As a Model Organic Redox Active Compound for Nonaqueous Flow Batteries. *J. Power Sources*, **327**, 151 (2016).
49. X. Wei et al. TEMPO-based catholyte for high-energy density nonaqueous redox flow batteries. *Adv. Mater.*, **26**, 7649 (2014).
50. N. G. Connelly and W. E. Geiger, Chemical Redox Agents for Organometallic Chemistry. *Chem. Rev.*, **96**, 877 (1996).
51. J. L. Barton, J. D. Milshtein, J. J. Hinricher, and F. R. Brushett, Quantifying the impact of viscosity on mass-transfer coefficients in redox flow batteries. *J. Power Sources*, **399**, 133 (2018).
52. J. A. Guin, D. P. Kessler, and R. A. Greenkorn, Average Pore Velocities in Porous Media. *Phys. Fluids*, **14**, 181 (1971).
53. I. V Zenyuk, D. Y. Parkinson, L. G. Connolly, and A. Z Weber, Gas-diffusion-layer structural properties under compression via X-ray tomography. *J. Power Sources*, **328**, 364 (2016).
54. A. M. Pezeshki, R. L. Sacci, G. M. Veith, T. A. Zawodzinski, and M. M. Mench, The Cell-in-Series Method: A Technique for Accelerated Electrode Degradation in Redox Flow Batteries. *J. Electrochem. Soc.*, **163**, A5202 (2016).
55. J. Friedl and U. Stimming, Determining Electron Transfer Kinetics at Porous Electrodes. *Electrochim. Acta*, **227**, 235 (2017).
56. A. J. Bard et al. *ELECTROCHEMICAL METHODS Fundamentals and Applications. Electrochemistry*, I. Faulkner and R. Larry, (1944).
57. A. M. Pezeshki, J. T. Clement, G. M. Veith, T. A. Zawodzinski, and M. M. Mench, High performance electrodes in vanadium redox flow batteries through oxygen-enriched thermal activation. *J. Power Sources*, **294**, 333 (2015).
58. C. N. Sun, F. M. Delnick, L. Baggetto, G. M. Veith, and T. A. Zawodzinski, Hydrogen evolution at the negative electrode of the all-vanadium redox flow batteries. *J. Power Sources*, **248**, 560 (2014).
59. R. W. Atkinson, Y. Garsany, B. D. Gould, K. E. Swider-Lyons, and I. V. Zenyuk, The Role of Compressive Stress on Gas Diffusion Media Morphology and Fuel Cell Performance. *ACS Appl. Energy Mater.*, acsaem.7b00077 (2017).
60. J. Kozeny, Über kapillare Leitung des Wassers im Boden. *Akad. Wiss.Wien*, **136**, 271 (1927).
61. A. Lamibrac et al. Characterization of Liquid Water Saturation in Gas Diffusion Layers by X-Ray Tomographic Microscopy. *J. Electrochem. Soc.*, **163**, F202 (2016).
62. A. Forner-Cuenca et al. Advanced Water Management in PEFCs: Diffusion Layers with Patterned Wettability: III. Operando characterization with neutron radiography. *J. Electrochem. Soc.*, **163**, F1389 (2016).
63. A. Forner-Cuenca et al. Advanced Water Management in PEFCs: Diffusion Layers with Patterned Wettability: II. Measurement of Capillary Pressure Characteristic with Neutron and Synchrotron Imaging. *J. Electrochem. Soc.*, **163**, F1038 (2016).
64. D. Zhang et al. Investigation of Porous Electrodes for Redox Flow Batteries through a combination of Computed Tomography, Lattice-Boltzmann modeling, and flow cell experiments. *Under Rev. J. Power Sources*,

65. T. J. Rabbow and A. H. Whitehead, Deconvolution of electrochemical double layer capacitance between fractions of active and total surface area of graphite felts. *Carbon N. Y.*, (2017).
66. K. J. Kim et al. A new strategy for integrating abundant oxygen functional groups into carbon felt electrode for vanadium redox flow batteries. *Sci. Rep.*, **4**, 1 (2014).
67. A. W. Bayeh et al. Ta_2O_5 -nanoparticle-modified graphite felt as a high-performance electrode for vanadium redox flow battery. *ACS Sustain. Chem. Eng.*, acssuschemeng.7b02752 (2018).
68. Y. Xiang and W. A. Daoud, Cr_2O_3-modified graphite felt as a novel positive electrode for vanadium redox flow battery. *Electrochim. Acta*, (2018).
69. O. Nibel et al. Performance of Different Carbon Electrode Materials: Insights into Stability and Degradation under Real Vanadium Redox Flow Battery Operating Conditions. *J. Electrochem. Soc.*, **164**, A1608 (2017).
70. M. A. Goulet, M. Skyllas-Kazacos, and E. Kjeang, The importance of wetting in carbon paper electrodes for vanadium redox reactions. *Carbon N. Y.*, **101**, 390 (2016).
71. R. Tahery, H. Modarress, and J. Satherley, Density and surface tension of binary mixtures of acetonitrile + 1-alkanol at 293.15 K. *J. Chem. Eng. Data*, **51**, 1039 (2006).
72. I. S. Khattab, F. Bandarkar, M. A. A. Fakhree, and A. Jouyban, Density, viscosity, and surface tension of water+ethanol mixtures from 293 to 323K. *Korean J. Chem. Eng.*, **29**, 812 (2012).
73. O. A. Ibrahim and E. Kjeang, Leveraging co-laminar flow cells for non-aqueous electrochemical systems. *J. Power Sources*, (2018).
74. J. T. Gostick, M. W. Fowler, M. D. Pritzker, M. A. Ioannidis, and L. M. Behra, In-plane and through-plane gas permeability of carbon fiber electrode backing layers. *J. Power Sources*, **162**, 228 (2006).
75. Z. Zeng and R. Grigg, A criterion for non-darcy flow in porous media. *Transp. Porous Media*, **63**, 57 (2006).
76. G. S. Beavers and E. M. Sparrow, Non-Darcy Flow Through Fibrous Porous Media. *J. Appl. Mech.*, **36**, 711 (1969).
77. L. Jr. Green and P. Duwez, Fluid flow through porous metals. *J. Appl. Mech.*, 39 (1951).
78. V. a. Jambhekar, Forchheimer Porous-media Flow Models - Numerical Investigation and Comparison with Experimental Data. 85 (2011).
79. T. H. Chilton and A. P. Colburn, II–Pressure Drop in Packed Tubes. *Ind. Eng. Chem.*, **23**, 913 (1931).
80. A. El-kharouf, T. J. Mason, D. J. L. Brett, and B. G. Pollet, Ex-situ characterisation of gas diffusion layers for proton exchange membrane fuel cells. *J. Power Sources*, **218**, 393 (2012).
81. J. P. Feser, A. K. Prasad, and S. G. Advani, Experimental characterization of in-plane permeability of gas diffusion layers. *J. Power Sources*, **162**, 1226 (2006).
82. S. Hasanpour, M. Hoorfar, and A. B. Phillion, Characterization of transport phenomena in porous transport layers using X-ray microtomography. *J. Power Sources*, **353**, 221 (2017).
83. J. G. Pharoah, On the permeability of gas diffusion media used in PEM fuel cells. *J. Power Sources*, **144**, 77 (2005).
84. E. C. Montoto, G. Nagarjuna, J. S. Moore, and J. Rodríguez-López, Redox Active Polymers for Non-Aqueous Redox Flow Batteries: Validation of the Size-Exclusion Approach. *J. Electrochem. Soc.*, **164**, A1688 (2017).
85. T. Suga, Y. J. Pu, K. Oyaizu, and H. Nishide, Electron-transfer kinetics of nitroxide radicals as an electrode-active material. *Bull. Chem. Soc. Jpn.*, **77**, 2203 (2004).
86. Q. Fu, Z. Zhang, W. Lin, and J. Huang, Single-electron-transfer nitroxide-radical-coupling reaction at ambient temperature: Application in the synthesis of block copolymers. *Macromolecules*, **42**, 4381 (2009).
87. G. Paasch, K. Micka, and P. Gersdorf, Theory of the electrochemical impedance of macrohomogeneous porous electrodes. *Electrochim. Acta*, (1993).
88. A. Bard, L. , Faulkner, Allen J Bard, and Larry R. Faulkner, *Electrochemical Methods: Fundamentals and Applications*, New York: Wiley, 2001. *Russ. J. Electrochem.* (2002).
89. R. O'Hayre, S. Cha, W. Colella, and F. B. Prinz, Fuel Cell Fundamental, Chapter 3: Fuel Cell Reaction Kinetics. *Fuel Cell Fundamentals*, (2016).
90. R. O'Hayre, S.-W. Cha, W. Colella, and F. B. Prinz, Chapter 5: Fuel Cell Mass Transport. *Fuel Cell Fundam.* 167 (2016).
91. V. P. Nemani and K. C. Smith, Uncovering the role of flow rate in redox-active polymer flow batteries: simulation of reaction distributions with simultaneous mixing in tanks. *Electrochim. Acta*, (2017).
92. X. Ma, H. Zhang, C. Sun, Y. Zou, and T. Zhang, An optimal strategy of electrolyte flow rate for vanadium redox flow battery. *J. Power Sources*, (2012).
93. A. A. Wong, M. J. Aziz, and S. Rubinstein, Direct Visualization of Electrochemical Reactions and Comparison of Commercial Carbon Papers in operando by Fluorescence Microscopy Using a Quinone-Based Flow Cell. *ECS Trans.* **77**, 153 (2017).
94. C. N. Sun, M. M. Mench, and T. A. Zawodzinski, High Performance Redox Flow Batteries: An Analysis of the Upper Performance Limits of Flow Batteries Using Non-aqueous Solvents. *Electrochim. Acta*, (2017).
95. L. Holzer et al. Microstructure-property relationships in a gas diffusion layer (GDL) for Polymer Electrolyte Fuel Cells, Part I: effect of compression and anisotropy of dry GDL. *Electrochim. Acta*, **227**, 419 (2017).
96. P. A. García-Salaberri et al. Analysis of representative elementary volume and through-plane regional characteristics of carbon-fiber papers: diffusivity, permeability and electrical/thermal conductivity. *Int. J. Heat Mass Transf.*, **127**, 687 (2018).
97. N. Zamel and X. Li, Effective transport properties for polymer electrolyte membrane fuel cells - With a focus on the gas diffusion layer. *Prog. Energy Combust. Sci.*, **39**, 111 (2013).
98. L. Hao and P. Cheng, Lattice Boltzmann simulations of anisotropic permeabilities in carbon paper gas diffusion layers. *J. Power Sources*, **186**, 104 (2009).
99. M. Wang et al. Numerical evaluation of the effect of mesopore microstructure for carbon electrode in flow battery. *J. Power Sources*, **424**, 27 (2019).